Associations of cortical iron accumulation with cognition and cerebral atrophy in Alzheimer's disease

Aocai Yang[1,2#], Lei Du[3#], Wenwen Gao[1,4], Bing Liu[1,2], Yue Chen[1,4], Yige Wang[1,2], Xiuxiu Liu[1,4], Kuan Lv[1,4], Wenwei Zhang[5], Hui Xia[5], Kai Wu[6], Guolin Ma[1,2]

[1]Department of Radiology, China-Japan Friendship Hospital, Beijing, China; [2]Graduate School of Peking Union Medical College, Chinese Academy of Medical Sciences and Peking Union Medical College, Beijing, China; [3]Department of Radiology, Key Laboratory of Carcinogenesis and Translational Research (Ministry of Education), Peking University Cancer Hospital & Institute, Beijing, China; [4]Peking University China-Japan Friendship School of Clinical Medicine, Beijing, China; [5]Institute of Electrical Engineering, Chinese Academy of Sciences, Beijing, China; [6]School of Biomedical Sciences and Engineering, South China University of Technology, Guangzhou, China

Contributions: (I) Conception and design: A Yang, L Du, H Xia, K Wu, G Ma; (II) Administrative support: G Ma; (III) Provision of study materials or patients: All authors; (IV) Collection and assembly of data: A Yang, L Du, W Gao, B Liu, Y Chen, Y Wang, X Liu, W Zhang, L Kuan; (V) Data analysis and interpretation: A Yang, L Du, H Xia, K Wu, G Ma; (VI) Manuscript writing: All authors; (VII) Final approval of manuscript: All authors.

#These authors contributed equally to this work and should be considered as first authors.

Correspondence to: Guolin Ma, PhD. Department of Radiology, China-Japan Friendship Hospital, No. 2 East Yinghua Road, Chaoyang District, Beijing 100029, China. Email: maguolin1007@qq.com.

Background: In Alzheimer's disease (AD), cerebral iron accumulation colocalizes with the pathological proteins amyloid-β (Aβ) and tau. Furthermore, tau-induced cortical thinning is associated with cognitive decline. In this study, quantitative susceptibility mapping (QSM) was used to investigate the whole-brain distribution pattern of cortical iron deposition and its relationships with cognition and cortical thickness in AD.

Methods: This cross-sectional study prospectively recruited 30 participants with AD and 26 age- and sex-matched healthy controls (HCs). All participants underwent QSM and T_1-weighted examinations on a 3.0T MRI scanner. Global cognition was assessed using the Mini-Mental State Examination (MMSE) and Montreal Cognitive Assessment (MoCA). Whole-brain cross-sectional QSM analysis and whole-brain QSM regression analyses against the MMSE and MoCA scores were performed. Surface-based morphometry analysis was also performed. Subsequently, in regions with significant atrophy, magnetic susceptibility was compared between the AD and HC groups, and the association between magnetic susceptibility and cortical thickness was assessed.

Results: Whole-brain QSM cross-sectional analysis in the AD group demonstrated widespread increased susceptibility across the cortical ribbon, asymmetrically covering the left hemisphere cerebral cortex, caudate nucleus, putamen, and partial cerebellar cortex. Whole-brain QSM regression analyses in the AD group showed that increased susceptibility covaried with lower MMSE and MoCA scores, and was predominantly located in the right parietal cortex and lateral occipital cortex. In the AD group, cortical thickness was reduced in the left superior temporal gyrus, right frontal pole, fusiform gyrus, and pars opercularis, and there were increases in susceptibility in the right frontal pole (AD: mean ± SD 0.034±0.007 ppm, 95% CI: 0.032–0.037 ppm; HC: 0.030±0.005 ppm, 95% CI: 0.028–0.032 ppm; P=0.016) and pars opercularis (AD: 0.020±0.003 ppm, 95% CI: 0.018–0.021 ppm; HC: 0.017±0.002 ppm, 95% CI: 0.017–0.018 ppm; P=0.002). Susceptibility was negatively correlated with cortical thickness in the right pars opercularis in the entire cohort (r=–0.521, P<0.001) and AD group (r=–0.510, P=0.005).

Conclusions: Widespread cortical iron, as measured by QSM, accumulated in AD and iron deposition was associated with poor cognitive performance. Increased iron content was also associated with brain

atrophy. Our study suggests QSM may be a useful imaging biomarker for monitoring the neurodegenerative progression of AD.

Introduction

Alzheimer's disease (AD) is one of the most common neurodegenerative diseases in older people. Manifestations of AD include progressive memory loss and, eventually, severe cognitive and behavior impairments (1). Excessive accumulation of amyloid-β (Aβ) plaques and tau neurofibrillary tangles in the brain gray matter are widely considered to be the pathological hallmarks of AD (2). Previous histochemical studies have shown that iron deposition is associated with Aβ plaques and tau neurofibrillary tangles, and can contribute to the formation and aggregation of Aβ and hyperphosphorylated tau (3-5). Furthermore, iron accumulation in insoluble amyloid plaques and neurofibrillary tangles is consistently observed in AD and has been extensively investigated (6). Iron, as the major metal element in the brain, plays an essential role in axon myelination, energetic metabolism, and neurotransmitter synthesis, and iron levels in specific brain regions, such as the basal ganglia, increase with age (7,8). The breakdown of iron homeostasis can cause various age-related neurodegenerative diseases (9). A previous study demonstrated that the neurotoxicity of oxidative stress induced by iron overload can promote neuron loss and degeneration (10). However, although the participation of iron in the pathogenic process of AD has been confirmed, the mechanism involved remains unknown.

Quantitative susceptibility mapping (QSM) is a magnetic resonance imaging (MRI) technique that uses an advanced approach to non-invasively quantify the magnetic susceptibility of tissue *in vivo* (11,12). Although susceptibility measured by QSM is non-specific and magnetic susceptibility can vary between different biophysical substances, such as iron, calcium, lipid, and myelin, paramagnetic iron is generally considered to be the predominant source of magnetic susceptibility in gray matter because the concentrations of other biophysical substances in the cortex are very low. Hence, studies of neurodegenerative diseases have always used QSM to evaluate iron content in the cortex (13).

Previous QSM studies have shown that excessive iron accumulates in several areas of the AD brain, including in some deep nuclei and cortical regions (14,15), and that increased QSM values are associated with cognitive decline in patients with AD (16). However, most QSM studies on AD have been limited to analysis of regions of interest, namely in the deep gray nuclei and some coarse cortical regions extracted from the standard brain atlases. As a data-driven method, voxel-based whole-brain analysis, which is not limited to predefined regions of interest, is able to explore the spatial specificity of magnetostatic changes in AD. However, voxel-based whole-brain studies exploring the spatial distribution of cortical iron accumulation and the associations between iron accumulation and cognition in AD are lacking.

Cortical atrophy, especially temporal and hippocampal atrophy, is one of the most prominent neuroimaging features of AD, and indicates considerable loss of neurons and synapses in the cerebral cortex. Because neuron loss is the main reason for cognitive decline and reflects the progression of neurodegeneration (17,18), understanding the relationship between cortical thickness and iron accumulation, and clarifying their effects on cognition, may provide new insights into the pathogenic mechanism of iron deposition in AD. However, to date, the association between cortical iron deposition and cortical thickness in AD has not been systematically investigated.

Using QSM, we conducted an *in vivo* study to explore the global distribution of cortical iron accumulation at the voxel level in patients with AD, and to locate the cortical regions in which magnetic susceptibility was correlated with cognition using a previously optimized whole-brain analysis workflow (19,20). We also performed a surface-based morphometry analysis using structural MRI to explore the hypothesis that iron content is increased in regions

with cortical atrophy in AD. Finally, we investigated the potential association between cortical thickness and iron content. We present the following article in accordance with the STROBE reporting checklist (available at https://qims.amegroups.com/article/view/10.21037/qims-22-7/rc).

Methods

Study participants

This study was conducted in accordance with the Declaration of Helsinki (as revised in 2013). The Ethics Committee of the China-Japan Friendship Hospital approved this prospective cross-sectional study. All participants were informed about the study and gave their written informed consent.

From November 2015 to March 2019, consecutive patients who met the diagnostic criteria for AD, as published by the National Institute of Neurological and Communicative Disorders and Stroke and the Alzheimer's Disease and Related Disorders Association (21), were recruited to the study from the Department of Neurology at the China-Japan Friendship Hospital. All patients recruited to the study completed integrated neuropsychological tests and MRI examinations. To be included in the study, patients needed to meet the following criteria: (I) age 50–85 years; (II) Fazekas scale score <2; and (III) ≥6 years of education. Global cognitive status was assessed by a senior neurologist using the Mini-Mental State Examination (MMSE) (22) and Montreal Cognitive Assessment (MoCA) test (23). Age- and sex-matched healthy controls (HCs) were recruited to the study from the local community. The cognitive status of HCs was assessed using the MMSE. The exclusion criteria for all participants were: (I) other neurologic and psychiatric diseases; (II) metabolic disease; (III) alcohol or drug abuse; (IV) MRI contraindications; and (V) abnormal findings on brain imaging.

MRI data acquisition

A Discovery MR750 3.0-T scanner (General Electric, Milwaukee, WI, USA) with an eight-channel head coil was used to perform MRI scans. The MRI examination consisted of an axial three-dimensional gradient-echo (3D-GRE) sequence and a sagittal three-dimensional T_1-weighted fast spoiled gradient-echo (3D-FSPGR) sequence. The 3D-GRE data were acquired using the following parameters: flip angle 12°; multiple echo times (TEs): TE1 3.19 ms, ΔTE 2.37 ms, and TE8 19.77 ms; repetition time

22.9 ms; bandwidth 62.5 Hz/pixel; slice thickness 1.0 mm; field of view 256 mm × 256 mm; voxel size 1×1×1 mm^3; and scan time 4.4 min. The 3D-FSPGR data were acquired using the following parameters: flip angle 12°; TE 2.9 ms; repetition time 6.7 ms; bandwidth 31.25 Hz/pixel; slice thickness 1.0 mm; field of view 256 mm × 256 mm; voxel size 1×1×1 mm^3; and scan time 4.17 min.

Reconstruction and post-processing of QSM data

The multi-echo phase and magnitude images acquired using the 3D-GRE sequence were used to reconstruct the QSM, following the default processing pipeline for 3D-GRE data in the Matlab-based STI Suite software (http://people.eecs.berkeley.edu/~chunlei.liu/software.html). First, the multi-echo phase images were unwrapped using Laplacian-based phase unwrapping (24), and the first-echo magnitude image was used to generate the binary brain mask using the brain extraction tool in FSL (https://fsl.fmrib.ox.ac.uk). Then, the variable-kernels sophisticated harmonic artifact reduction for phase data (V-SHARP) (25) method with the binary brain mask was used to remove the background frequency of the unwrapped phase image. The susceptibility map was estimated from the local field map using the streaking artifact reduction method for QSM (26).

The QSM post-processing steps and the whole-brain analysis were conducted using an optimized pipeline in QSMexplorer (https://gitlab.com/acostaj/QSMexplorer) (27). Briefly, a study-specific structural template was generated from the bias-corrected 3D-FSPGR images of all participants, following the "antsMultivariateTemplate Construction2" routine with six full runs in Advanced Normalization Tools (ANTs; http://stnava.githib.io/ANTs); simultaneously, the individual T_1-weighted structural images were spatially normalized to the template using the "SyN" approach in ANTs. Then, the first-echo magnitude images were corrected for bias field and rigidly coregistered to their corresponding T_1-weighted structural images. The QSM images were subsequently warped to the study-specific T_1-weighted template for spatial normalization through a method combining the above-mentioned transformations and third-order b-spline interpolation in ANTs. We also created a study-specific QSM template by averaging the normalized QSM images across the participants (*Figure 1*). In addition, the 3D-FSPGR images were segmented to obtain probabilistic maps of the gray matter for further analysis using the SPM12 software (http://www.fil.ion.ucl.ac.uk/spm/software/spm12).
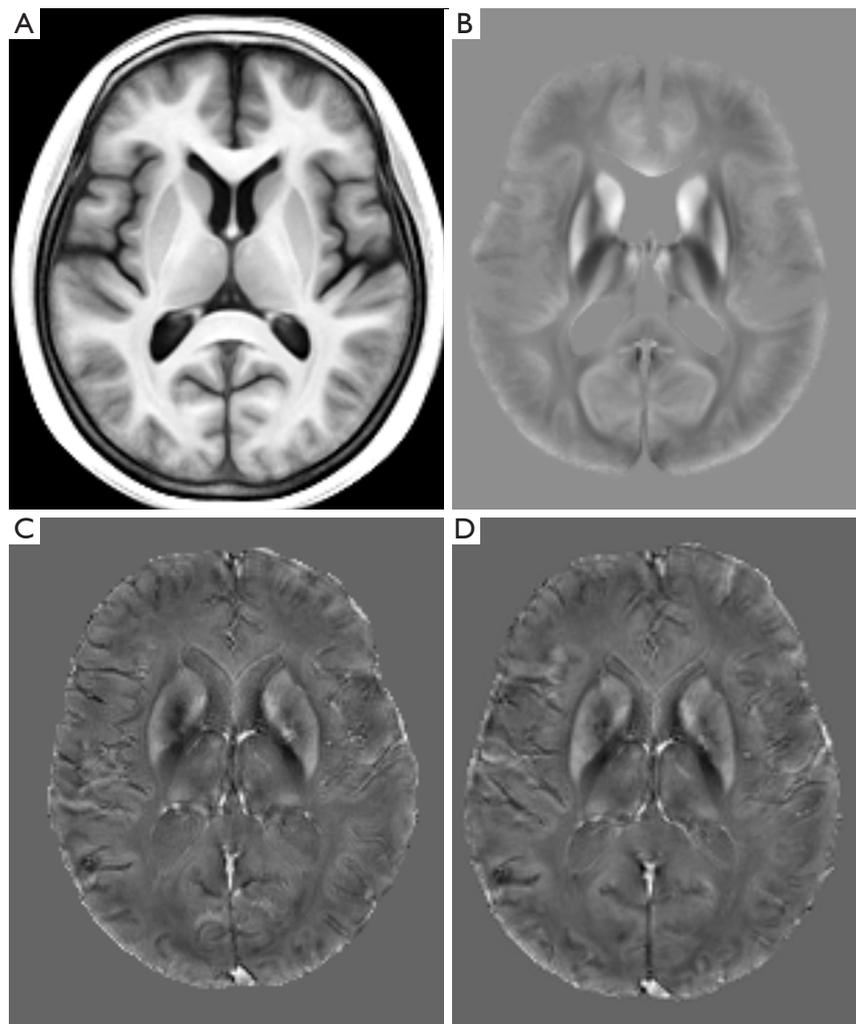
Figure 1 Study-specific templates and QSM spatial normalization. (A,B) Study-specific T_1-weighted structural (A) and QSM (B) templates. (C,D) Original (C) and spatial normalized (D) QSM of a 75-year-old woman with Alzheimer's disease. QSM, quantitative susceptibility mapping.

Post-processing of structural data

Cortical thickness was measured using T_1-weighted structural images. Following the standardized framework in FreeSurfer version 6.0.0 (http://surfer.nmr.mgh.harvard.edu), the post-processing routine included motion correction, volumetric segmentation, inflation, surface reconstruction, spherical registration, smoothing, visual inspection, and manual correction. Detailed descriptions of the post-processing methods have been described previously (28,29). Cortical thickness was measured as the vertical distance between the gray-white matter boundary and the pial surface.

Statistical analysis

Voxel-based whole-brain QSM analysis

Because our whole-brain analysis focused on the cortex and absolute QSM data have previously been proven to reduce the susceptibility spatial variance and spurious dispersion across the cortex (25), the absolute QSM value was used for whole-brain analysis and further regional analysis. To reduce the impact of inaccurate registration, the normalized QSM images were smoothed using a three-dimensional Gaussian kernel with a standard deviation of 3 mm, and additional smoothing compensation was performed using the smoothed gray matter mask to improve the specificity of
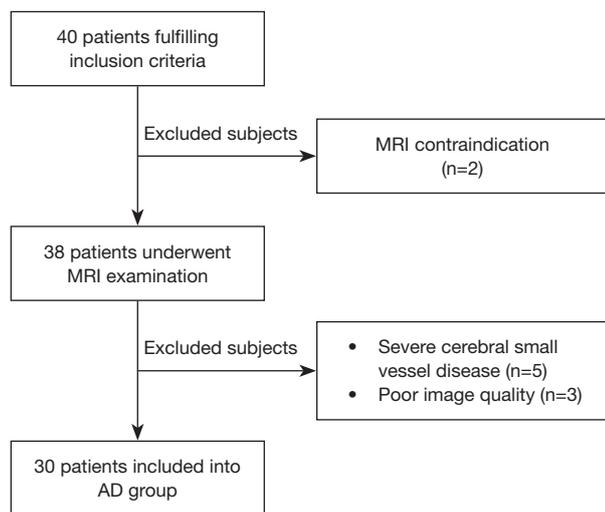
Figure 2 Flowchart showing the selection of patients with AD for this study. MRI, magnetic resonance imaging; AD, Alzheimer's disease.

the statistical analysis in the cortex (30).

Because the absolute QSM value (absolute susceptibility) varies by age (27,30,31), age was included as a covariate in all subsequent statistical models. We performed voxel-based cross-sectional QSM analysis to explore intergroup differences in absolute susceptibility between patients with AD and HCs, in which sex and age were both mean-centered and corrected as nuisance covariates. Also, whole-brain QSM regression analyses against MMSE and MoCA scores were performed to evaluate correlations between absolute susceptibility and cognition in the AD group. The whole-brain statistical analyses for each design matrix were assessed by randomized permutation tests (10,000 permutations) with a threshold-free cluster enhancement algorithm (TFCE) in FSL (http://fsl.fmrib.ox.ac.uk/fsl/fslwiki/Randomise); these calculations were restricted to the gray matter mask. The statistical significance threshold was set to a family-wise error (FWE)-corrected P<0.05.

Finally, for visualization purposes and further regional analysis, study-specific templates and resultant statistical maps were warped into the Montreal Neurological Institute (MNI) space.

Cortical thickness analysis

To explore intergroup differences in cortical thickness, surface-based morphometry analysis was performed using the "mri_glmfit" module in FreeSurfer, with adjustment for age and sex in the "Different-Offset, Same-Slope" general linear model. For multiple comparison correction, a Z-based Monte Carlo simulation algorithm was implemented, with a vertex-wise threshold of P<0.01 (unsigned) and a cluster-wise threshold of P<0.05. After multiple comparison correction, the cortical thicknesses of significant clusters were extracted from the surface images of all participants.

Also, the surface labels of significant clusters were transformed into a volume mask and then warped into the MNI space; subsequently, the mean absolute susceptibility of all participants in the corresponding atrophied regions was extracted by using the "fslmeants" tool in FSL.

Other statistical analyses

All other statistical analyses were conducted using SPSS version 21.0 (IBM Corp., Armonk, NY, USA), with graphs drawn using GraphPad Prism 8 (GraphPad Software, San Diego, CA, USA). The Shapiro–Wilk test was used to assess the normality of data distribution. Sequential data are presented as the mean ± SD. Student's t-test and the chi-squared (χ^2) test were used to assess the significance of differences in clinical characteristics. The significance of differences in the absolute QSM values of atrophied regions between groups was assessed using the Mann-Whitney U test. Correlations between cortical thickness and absolute QSM values in atrophied regions were assessed by partial correlation analysis while controlling for age. The Benjamini-Hochberg false discovery rate method was used for multiple comparison correction. According to the results of cortical thickness analysis, there were four significantly atrophied regions when the false discovery rate significance threshold was set to q<0.05.

Results

Demographic characteristics of participants

Thirty AD patients (mean age 68.5±6.8 years; 21 women) and 26 HCs (mean age 65.5±8.1 years; 19 women) were recruited to the study. A flowchart of the selection process for the AD group is shown in *Figure 2*. There were no significant differences in age or sex between the AD and HC groups, and all participants were right-handed. The mean number of education years was higher in the AD than the HC group (P=0.015). The MMSE scores of the AD group were significantly lower than those of the HC group (P<0.001). The demographic and clinical characteristics of all participants are summarized in *Table 1*.

Table 1 Demographic and clinical characteristics of the study cohort

Characteristics	AD group (n=30)	HC group (n=26)	P value
Sex (No. males/females)	9/21	7/19	0.799
Age (years)	68.5±6.8	65.5±8.1	0.136
Education (years)	11.33±3.86	8.50±4.57	0.015
MMSE score	19.77±4.79	27.96±1.64	<0.001
MoCA score	16.87±4.5	NA	NA

Unless indicated otherwise, data are given as the mean ± SD. AD, Alzheimer's disease; HC, healthy control; MMSE, Mini-Mental State Examination; MoCA, Montreal Cognitive Assessment; NA, not applicable.

Whole-brain cortical QSM cross-sectional analysis

Whole-brain cross-sectional analysis revealed that relative to the HCs, the AD group had widespread increased absolute susceptibility along the cortical ribbon, predominantly in the left cerebral cortex, which reflected increased iron content. Abnormalities on the left side were found in frontal lobe structures including the superior frontal gyrus, middle frontal gyrus, inferior frontal gyrus, frontal pole, and precentral gyrus; in parietal lobe structures encompassing the precuneus cortex, postcentral gyrus, supramarginal gyrus, and angular gyrus; in temporal lobe structures including the inferior temporal gyrus, middle temporal gyrus, fusiform gyrus, and parahippocampal gyrus; in occipital lobe structures, primarily the lateral occipital cortex and occipital pole; and in the insula cortex, opercular cortex, and cingulate cortex (P<0.05, FWE-corrected). Deep gray matter nuclei located in the basal ganglia, including the left caudate and putamen nuclei, were also found to be involved. In the AD group, although absolute susceptibility was primarily increased in the left cerebral cortex, extensively covering the left frontal, parietal, temporal, and occipital lobes, the right cerebral cortex also had relatively sparse regions with abnormally increased absolute susceptibility, including the right precuneus cortex, cingulate gyrus, lateral occipital cortex, occipital pole, insular cortex, opercular cortex, postcentral gyrus, precentral cortex, and supramarginal gyrus (P<0.05, FWE-corrected). Notably, the susceptibility of the Crus II, VIIb, and VIIIa regions in the left cerebellar cortex was also significantly increased in the AD group (P<0.05, FWE-corrected). No significant clusters of decreased absolute QSM values were found in the AD group. The peak MNI coordinates and anatomical labeling of significant clusters with increased absolute susceptibility are presented in *Table 2* and *Figure 3*, respectively.

Whole-brain cortical QSM regression analysis

Whole-brain QSM regression analysis with cognition showed that, in patients with AD, increased absolute susceptibility in the right angular gyrus, supramarginal gyrus, lateral occipital cortex, parietal operculum cortex, left frontal operculum cortex, and inferior frontal gyrus was associated with decreased MMSE scores (*Figure 4A*; *Table 3*; TFCE, FWE-corrected P<0.05). Increased susceptibility in the right angular gyrus, supramarginal gyrus, lateral occipital cortex, superior temporal gyrus, left superior frontal gyrus, inferior frontal gyrus, and frontal pole was also associated with decreased MoCA scores in patients with AD (*Figure 4B*; *Table 3*; TFCE, FWE-corrected P<0.05). Interestingly, similar patterns were seen in maps of whole-brain QSM regression analysis plotted against MoCA scores and against MMSE scores. However, unlike those of cross-sectional analysis, the results of QSM regression analysis with cognition were primarily located in the right hemisphere.

In contrast, we did not find any significant clusters in which absolute susceptibility was positively correlated with the MMSE or MoCA score at the whole-brain level.

Atrophy measurements

The results of surface-based morphometry analysis revealed reduced cortical thickness in several regions in the AD group, including the left superior temporal gyrus (AD: 2.74±0.28 mm, 95% CI: 2.63–2.84 mm; HC: 3.01±0.16 mm, 95% CI: 2.94–3.07 mm), right fusiform gyrus (AD: 2.76±0.31 mm, 95% CI: 2.64–2.87 mm; HC: 3.11±0.20 mm, 95% CI: 3.03–3.19 mm), pars opercularis (AD: 2.42±0.17 mm, 95% CI: 2.36–2.49 mm; HC: 2.63±0.13 mm, 95% CI: 2.58–2.67 mm), and frontal pole (AD: 2.30±0.23 mm, 95% CI: 2.21–2.38 mm; HC: 2.55±0.21 mm, 95% CI: 2.47–2.63 mm) (Monte Carlo null-Z simulation-corrected P<0.05; *Figure 5*; *Table 4*). At

4576

Yang et al. Iron deposition related to cognition and brain atrophy in AD

Table 2 Clusters showing significant differences in cortical absolute susceptibility between the AD and HC groups

Brain regions of significant clusters	Cluster size (voxels)	P_FWE value	Peak MNI coordinates (mm)			Absolute susceptibility (ppm)	
			X	Y	Z	AD	HC
Contrast: AD > HC							
LH frontal lobe/parietal lobe/temporal lobe/insula/ caudate/putamen	18,795	0.002	−55	−6	8	0.027±0.004	0.022±0.002
LH Crus II/VIIb	4,142	0.016	−21	−77	−47	0.018±0.004	0.014±0.004
LH lateral occipital cortex/occipital pole/middle temporal gyrus/inferior temporal gyrus	3,681	0.005	−49	−74	−7	0.029±0.004	0.025±0.03
LH inferior temporal gyrus/fusiform cortex/ parahippocampal gyrus	2,682	0.009	−39	−45	−25	0.038±0.008	0.031±0.005
LH precuneus cortex/cingulate gyrus	2,433	0.006	−7	−42	41	0.021±0.003	0.018±0.002
RH precuneus cortex/cingulate gyrus	2,123	0.012	5	−46	41	0.021±0.003	0.017±0.002
RH lateral occipital cortex/occipital pole	1,479	0.003	31	−76	17	0.025±0.005	0.020±0.002
LH superior frontal gyrus/middle frontal gyrus/ precentral gyrus	1,230	0.032	−20	4	51	0.022±0.006	0.018±0.003
LH cerebellar VIIIa/VIIIb	676	0.030	−22	−46	−46	0.030±0.005	0.026±0.004
RH insular cortex	605	0.033	37	2	9	0.026±0.005	0.022±0.004
LH postcentral gyrus/precentral gyrus	350	0.006	−41	−27	53	0.031±0.008	0.025±0.005
RH postcentral gyrus/supramarginal gyrus/ opercular cortex	273	0.020	62	−17	22	0.021±0.003	0.018±0.002
LH postcentral gyrus	194	0.006	−53	−12	33	0.022±0.004	0.019±0.002
RH central opercular cortex	179	0.043	53	2	9	0.019±0.005	0.015±0.002
LH postcentral gyrus/supramarginal gyrus	176	0.032	−42	−33	50	0.020±0.005	0.017±0.003
RH precentral gyrus	96	0.042	55	7	26	0.023±0.005	0.019±0.003
RH postcentral gyrus	83	0.018	44	−29	51	0.021±0.005	0.016±0.003
LH supramarginal gyrus	50	0.038	−57	−46	29	0.020±0.004	0.017±0.003
LH middle frontal gyrus	39	0.019	−35	21	37	0.021±0.006	0.017±0.004

Unless indicated otherwise, data are given as the mean ± SD. Clusters larger than 30 voxels are listed. AD, Alzheimer's disease; HC, healthy control; FWE, family-wise error; MNI, Montreal Neurological Institute; LH, left hemisphere; RH, right hemisphere.

the whole-brain level, cortical thickness was not found to be statistically significantly higher in the AD group than the HC group.

Correlation between QSM and cortical thickness

Further analysis in atrophied regions showed that absolute susceptibility in the right frontal pole (AD: 0.034±0.007 ppm, 95% CI: 0.032–0.037; HC: 0.030±0.005 ppm, 95% CI: 0.028–0.032; P=0.016) and right pars opercularis (AD: 0.020±0.003 ppm, 95% CI: 0.018–0.021; HC: 0.017±0.002 ppm, 95% CI:

0.017–0.018; P=0.002) was significantly higher in the AD group than the HC group after FDR correction. However, there was no significant difference in absolute susceptibility between the two groups in the left superior temporal gyrus (AD: 0.027±0.004 ppm, 95% CI: 0.026–0.029; HC: 0.026±0.003 ppm, 95% CI: 0.024–0.027; P=0.168) and right fusiform gyrus (AD: 0.039±0.006 ppm, 95% CI: 0.037–0.041; HC: 0.036±0.004 ppm, 95% CI: 0.034–0.037; P=0.057) (*Figure 6A*). The results of partial correlation analysis between QSM values and cortical thickness showed that, in the AD group, absolute susceptibility was significantly negatively correlated with cortical thickness in the right pars
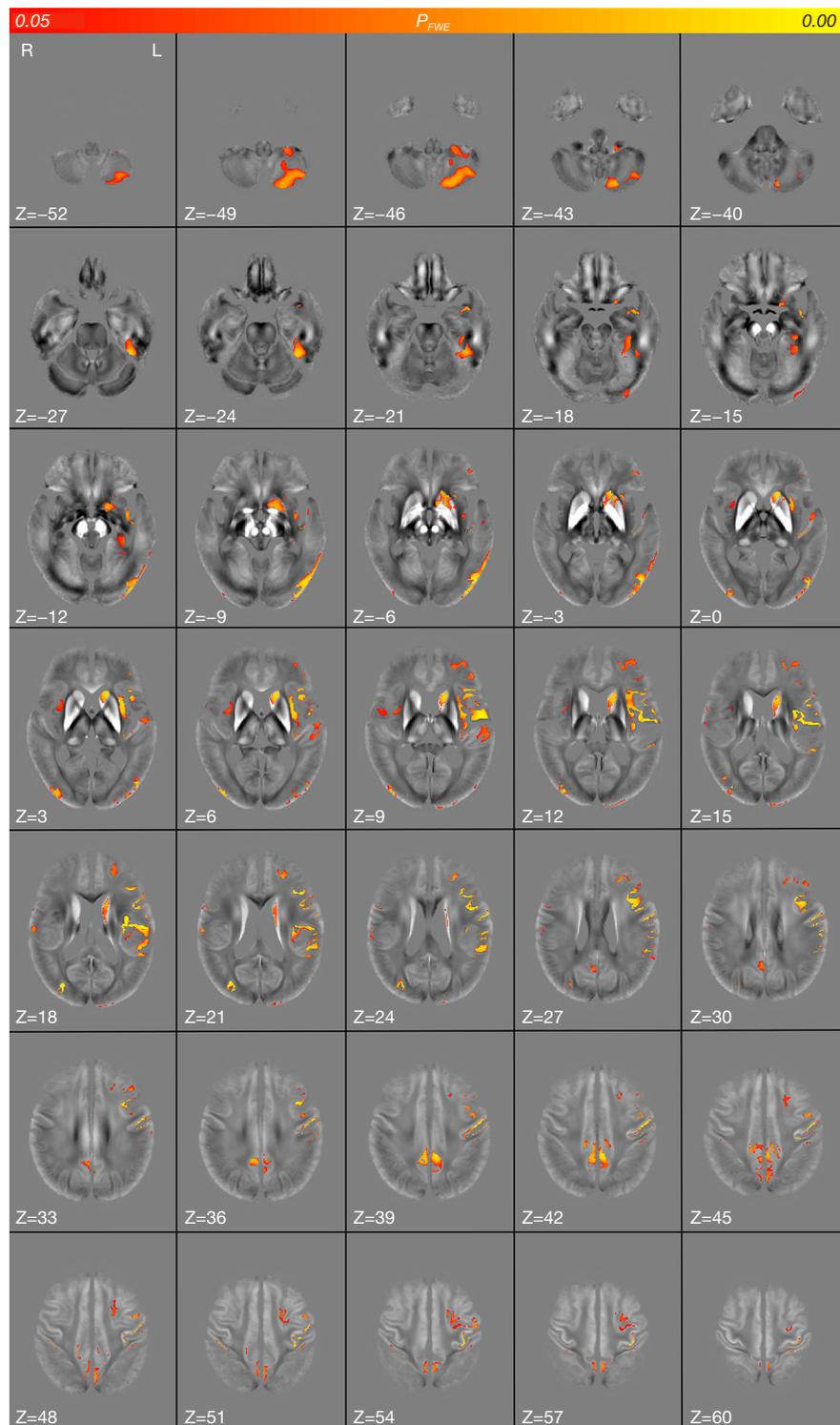
Figure 3 Results from whole-brain absolute QSM analysis. Red-yellow clusters represent significantly higher absolute susceptibility in the AD group than in the HC group (threshold-free cluster enhancement, family-wise error-corrected P<0.05). The resulting maps are overlaid onto the study-specific QSM template in the Montreal Neurological Institute coordinate system. R, right; L, left; QSM, quantitative susceptibility mapping; AD, Alzheimer's disease; HC, healthy control.

Figure 4 Results from whole-brain absolute QSM regression analysis against the MMSE and MoCA scores in AD. (A) Red-yellow clusters represent significant negative associations between cortical absolute susceptibility and the MMSE score in the AD group (TFCE, FWE-corrected P<0.05). (B) Blue clusters represent significant negative associations between cortical absolute susceptibility and MoCA scores in the AD group (TFCE, FWE corrected P<0.05). Resulting maps are overlaid onto the study-wise QSM template in the Montreal Neurological Institute coordinate system. R, right; L, left; QSM, quantitative susceptibility mapping; MMSE, Mini-Mental State Examination; MoCA, Montreal Cognitive Assessment; AD, Alzheimer's disease; TFCE, threshold-free cluster enhancement; FWE, family-wise error.

Table 3 Significant clusters in the whole-brain absolute susceptibility regression against the MMSE and MoCA scores

Brain region	Cluster size (voxels)	P$_{FWE}$ value	Peak MNI coordinates (mm)		
			X	Y	Z
MMSE (negative linear relationship)					
RH angular gyrus/supramarginal gyrus	2,649	0.015	56	−46	36
RH lateral occipital cortex	533	0.033	40	−72	28
RH parietal operculum cortex	107	0.048	42	−25	22
LH frontal operculum cortex/inferior frontal gyrus	82	0.037	−33	28	6
RH lateral occipital cortex	56	0.047	32	−65	35
RH supramarginal gyrus/angular gyrus	30	0.023	45	−47	50
MoCA (negative linear relationship)					
RH angular gyrus/supramarginal gyrus	2,810	0.008	52	−52	26
LH superior frontal gyrus	367	0.036	−12	33	56
RH lateral occipital cortex	294	0.038	45	−70	27
LH frontal pole/superior frontal gyrus	281	0.035	−18	37	30
LH frontal operculum cortex/inferior frontal gyrus	188	0.023	−34	28	6
RH superior temporal gyrus	77	0.041	67	−33	12
RH angular gyrus/supramarginal gyrus	30	0.031	45	−47	50

Clusters larger than 30 voxels are listed. FWE, family-wise error; LH, left hemisphere; MMSE, Mini-Mental State Examination; MNI, Montreal Neurological Institute; MoCA, Montreal Cognitive Assessment; RH, right hemisphere.
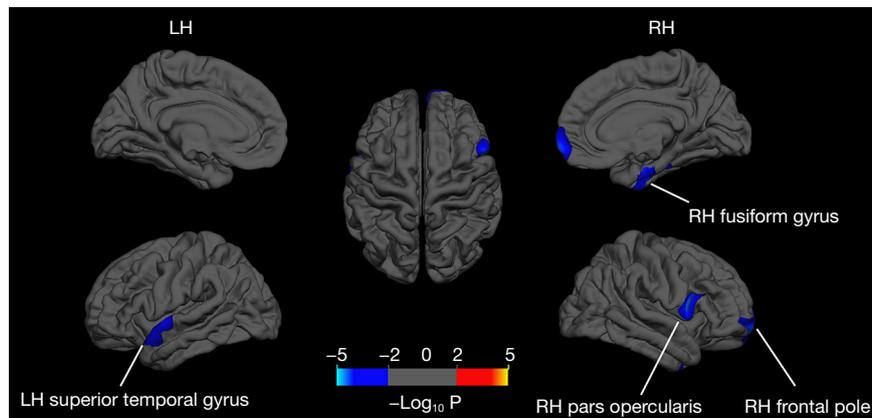

Figure 5 Results from whole-brain vertex-wise cortical thickness analysis. Compared with the HC group, cortical thickness was significant reduced in the AD group in the superior temporal gyrus in the LH, as well as the fusiform gyrus, pars opercularis, and frontal pole in the RH (cluster-wise, Z-based Monte Carlo simulation-corrected P<0.05). Original statistical maps are overlaid on the FreeSurfer average pial surface, and are shown in blue. HC, healthy control; AD, Alzheimer's disease; LH, left hemisphere; RH, right hemisphere.

opercularis (r=−0.510, P=0.005) after FDR correction (*Figure 6B*). For the whole study cohort, absolute susceptibility was inversely correlated with cortical thickness in the atrophied regions of the right fusiform gyrus (r=−0.436, P=0.001) and right pars opercularis (r=−0.521, P<0.001) after FDR correction (*Figure 6C*). However, the right frontal pole and the

4580

Yang et al. Iron deposition related to cognition and brain atrophy in AD

Table 4 Clusters showing significant differences in cortical thickness between the AD and HC groups

Brain region	Cluster size (mm²)	CWP	Peak MNI coordinates (mm)			Cortical thickness (mm)	
			X	Y	Z	AD	HC
Contrast: AD < HC							
LH superior temporal gyrus	707.14	0.0395	−55.4	−3.3	−4.0	2.74±0.28	3.01±0.16
RH fusiform gyrus	969.25	0.0070	37.8	−13.3	−28.7	2.76±0.31	3.11±0.20
RH frontal pole	825.01	0.0195	8.5	63.7	−9.2	2.30±0.23	2.55±0.21
RH pars opercularis	812.41	0.0209	49.9	11.7	12.6	2.42±0.17	2.63±0.13

AD, Alzheimer's disease; HC, healthy control; CWP, cluster-wise P value; MNI, Montreal Neurological Institute; LH, left hemisphere; RH, right hemisphere.
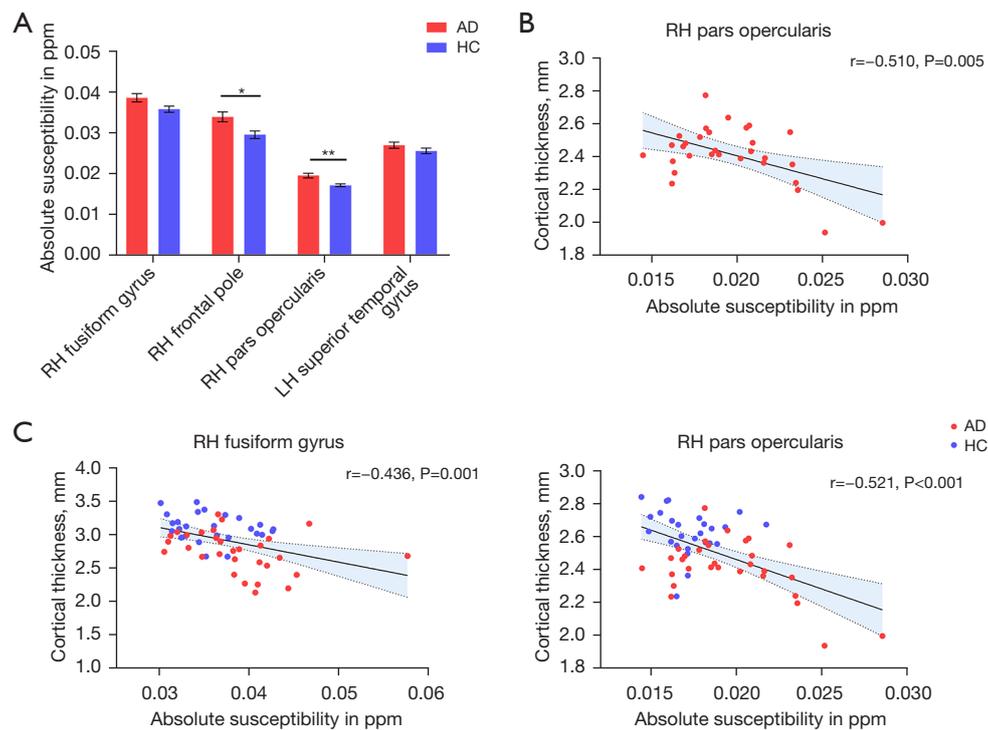

Figure 6 Absolute susceptibility in the Alzheimer's disease (AD) and healthy control (HC) groups and its correlation with cortical thickness in atrophied regions. (A) The absolute susceptibility of the RH frontal pole (P=0.016) and RH pars opercularis (P=0.002) was significantly higher in the AD than the HC group (FDR correction, P<0.05). Data are shown as the mean ± SEM. *P <0.05 (uncorrected), **P<0.01 (uncorrected). (B) In the AD group, absolute susceptibility was negatively correlated with cortical thickness in the atrophied region of the RH pars opercularis after FDR correction (r=−0.510, P=0.005). (C) In the whole cohort, absolute susceptibility was negatively correlated with cortical thickness in the atrophied regions of the RH fusiform gyrus (r=−0.436, P=0.001) and RH pars opercularis (r=−0.521, P<0.001) after FDR correction. Shaded areas indicate 95% confidence intervals. RH, right hemisphere; LH, left hemisphere; AD, Alzheimer's disease; HC, healthy control; FDR, false discovery rate.

left superior temporal gyrus showed no significant correlations between absolute susceptibility and cortical thickness in the whole cohort (right frontal pole: r=−0.183, P=0.182; left superior temporal gyrus: r=−0.191, P=0.162) or in the AD group (right frontal pole: r=0.013, P=0.945; left superior temporal gyrus: r=−0.285, P=0.134).

Discussion

Iron accumulation in the brain is consistently observed in AD. As the most crucial structural imaging characteristic of AD, cortical thinning is associated with cognitive impairment. However, the relationships of cortical iron content with cortical thickness and cognitive decline in AD remain unclear. In this study, we obtained a whole-brain pattern of susceptibility perturbations throughout the cortex and explored the association between susceptibility and cognitive severity in patients with AD. We also assessed the correlations between susceptibility and cortical thickness in these patients. Our main findings are that: (I) there was widespread increased susceptibility across the cortical ribbon in patients with AD, non-symmetrically covering the left cerebral cortex, deep gray-matter nuclei, and partial cerebellar cortex; (II) susceptibility was increased in the right parietal cortex and lateral occipital cortex in patients with AD, which correlated with cognitive deficits; and (III) increased susceptibility was associated with reduced cortical thickness in the right pars opercularis.

Whole-brain voxel-based analysis demonstrated increased susceptibility, which approximately reflected elevated iron content and was predominantly distributed in the cortex of left frontal, parietal, temporal, occipital and insula lobes, with some sparse clusters distributed in the right hemisphere. Excessive iron deposition in the AD brain is associated with Aβ plaques and tau neurofibrillary tangles, and has been extensively investigated. Iron has been proven to modulate the misfolding process associated with Aβ formation (32) and to be correlated with hyperphosphorylation of tau (33). Deposition of Aβ and tau appears to affect the medial parietal cortex, medial temporal lobe, and frontal lobe first, with aggregates gradually appearing in the whole brain cortex (34). However, the distribution patterns of Aβ and tau proteins during disease progression are not entirely the same. The accumulation of Aβ plaques begins in the temporal, occipital, and frontal lobes, and finally affects the striatum, brain stem nuclei, and cerebellum, whereas tau protein is preferentially deposited in the temporal and frontal lobes, and ultimately the entire cortex (35). Both Aβ plaques and tau tangles are deposited in the temporal lobe first, which is also the most affected brain area, and eventually aggregate in the striatal region and cerebellum. In the cerebral cortex, our resultant map showed that increased iron levels were highly colocalized with the cortical regions in which Aβ and tau are likely to first accumulate, especially in the temporal lobe; this may be indirect evidence of an association between iron deposition and neuritic plaques and neurofibrillary tangle aggregations. Previous imaging studies using Aβ positron emission tomography and QSM techniques reported that increased iron content was spatially colocalized with Aβ accumulation (36,37). A histological post-mortem study combined with T_2^*-weighted MRI found an association between iron and tau aggregations (35). Furthermore, an elevated iron content was found in left basal ganglia regions, including the left caudate and putamen nuclei, which is consistent with results from our previous study (14).

Because the voxel-based whole-brain analysis was limited to the gray matter, which was segmented by SPM12 from T_1-weighted anatomical data, and the probabilistic tissue map of the gray matter contained the basal ganglia, we did not repeat the regional analysis in the basal ganglia. Interestingly, we found that there was increased iron content in several regions of the cerebellum. A prior study used flutemetamol positron emission tomography and QSM to confirm that iron deposition in multiple brain regions, including the cerebellum, was highly correlated with the deposition of Aβ plaques in elderly patients (38). Another study using whole-brain regression analysis found that age-related iron deposition in healthy adults was spatially selective and that iron accumulated in the cerebellar cortex with aging (27). Our findings in the cerebellar cortex support the concept that iron homeostasis is disrupted and that physiological iron deposition is accelerated in the AD brain. Furthermore, after correction for multiple comparisons, clusters of significantly increased susceptibility were found primarily in the left hemisphere, and bilateral perturbations of susceptibility were found at lower thresholds. These findings illustrate the asymmetric patterns of iron deposition and its features of selective vulnerability, which are also seen in other diseases, such as Parkinson's disease (20).

Because the processes and mechanisms of iron overload in the AD brain are complex, neuritic plaques and neurofibrillary tangle aggregations may not be the only sources of iron elevation; for example, the increased blood-brain barrier permeability in AD could increase iron uptake in the brain (10,39). Furthermore, when excess Aβ accumulates in small blood vessels in the brain, it causes cerebral amyloid angiopathy (CAA), subsequently leading to CAA-related microhemorrhage and elevated iron concentrations in the cortex (40). Nearly all patients with AD have CAA to varying degrees (41). However, based on the results of the present cross-sectional study, we still do

not know whether abnormal iron homeostasis is a cause or consequence of AD, and we cannot determine the source of the iron. Nevertheless, our results provide a map of elevated iron distribution that may serve as a robust rationale for selecting regions of interest in future studies.

A previous study also demonstrated higher cortical iron using another iron-sensitive MRI technique, R2* mapping, in longitudinal and cross-sectional assessments (42). However, compared with other iron-sensitive MRI techniques, such as T_2*-weighted, R2*-, and susceptibility-weighted imaging, QSM provides the most precise method for tissue iron quantification. However, although QSM is highly sensitive to variations in brain iron content and is commonly equated with changes in brain iron content, the QSM signal is still not specific to iron and its accuracy can be affected by diamagnetic myelin. Therefore, whole-brain analyses in the present study were restricted to the cortical ribbon to reduce error variation resulting from opposite magnetic susceptibility in the gray and white matter. Furthermore, a previous study demonstrated a significant relationship between histologically quantitated iron values and QSM, thus confirming that magnetic susceptibility is suitable for iron quantification in the gray matter (43).

In the whole-brain cortical susceptibility regression analysis against the MMSE and MoCA scores, the resultant maps were almost the same for both scores, which reveals that susceptibility perturbations in these overlaid regions are highly sensitive and related to global cognition in patients with AD. In the AD group, we found increased susceptibility covaried with poor cognitive performance predominantly located in the right angular gyrus, supramarginal gyrus, and lateral occipital cortex, with some more sparse clusters in the left frontal cortex. The angular gyrus is linked to memory retrieval, attention, spatial cognition, word reading, and comprehension, whereas the supramarginal gyrus is linked to phonological processing and emotional responses (44,45). The lateral occipital cortex is associated with working memory, which is consistent with observations of memory, language, and emotional deficits in AD. In the present study, we showed, for the first time, that cognitive scores are negatively related to QSM signals detected at the voxel level in AD. However, those cognition-correlated regions did not overlap with the resultant maps of increased susceptibility at the voxel level. One possible interpretation of this result is that the right angular gyrus, supramarginal gyrus, lateral occipital cortex, and left superior frontal gyrus are more sensitive to iron dysregulation in AD, even though the iron content in

these regions was not significantly higher than that in the HC group at the voxel level. Another explanation is that different cortical regions execute particular brain functions, but in the whole-brain regression analysis we only used the global cognitive score, rather than a specific cognitive score, to evaluate the relationship between susceptibility and cognitive impairment.

The results of the atrophy analysis demonstrated that conventional neuroimaging failed to identify atrophy in some regions in which QSM showed excessive iron deposition. Considering the cohort of patients with AD in the present study was relatively young and their cognitive impairment was not very severe, QSM may be more sensitive than conventional measurement to indicate abnormal conditions in the early stages of AD. There is strong evidence that ferric iron elevation interferes with the normal functions of microglial cells and mitochondria (46,47), which can disrupt normal cellular function and eventually lead to tissue damage and neurodegeneration. This effect could occur earlier than obvious atrophy captured by standard structural MRI.

Oxidative stress and a neuroinflammatory environment induced by iron overload can eventually cause cellular dysfunction, apoptosis, and ferroptosis, and ultimately lead to neuron death and loss, which may manifest as brain atrophy (48). In the present study, susceptibility in atrophied regions of the right frontal pole and right pars opercularis was significantly higher in the AD group than the HC group. Furthermore, in the atrophied region of the right pars opercularis, susceptibility was inversely correlated with cortical thickness. These results can be explained by the theory that disrupted iron homeostasis triggers neurotoxic events and causes neuron damage. Reduced cortical thickness in AD is primarily associated with tau aggregation rather than Aβ (49,50), and a recent study showed that iron deposition was spatially colocalized with tau rather than Aβ (51). Therefore, the results of the present study provide indirect evidence that overload iron with tau aggregation promotes the neurodegenerative process in AD. Also, increased susceptibility has been shown to have a significant modulatory effect on the relationship between tau, as determined by positron emission tomography, and cortical thickness in the inferior temporal gyrus in AD (52). A prior study reported that greater susceptibility was associated with lower cortical volume only in the medial temporal region (16); however, we did not find any significant relationships between greater susceptibility and thinner cortical thickness in the temporal cortex. The differences in results between

this study and others may due to differences in sample size and the region of interest selected. Although the exact pathogenic mechanism by which excessive iron contributes to neurodegeneration in AD remains unknown, elevated iron content is increasingly being recognized as a new therapeutic target for AD, and it has been shown that using an iron chelator can slow and reverse neurodegenerative progression in AD (53,54).

Limitations

This study has several limitations. First, the sample size of the study was small and we did not recruit amnestic subjects with mild cognitive impairment. Second, the QSM signal was interpreted as "iron content", but the current QSM technique cannot differentiate different metals and myelin in the brain. Second, we used the composite MMSE and MoCA scores to assess the relationships between global cognition and QSM signals, but we did not assess the relationships between QSM and the specific scores of different cognitive domains, such as the episodic memory score. Third, although the study recruited several patients with early onset AD, the number of these patients was not sufficient to allow for subgroup analysis. In future studies, we will increase the sample size to enable further subgroup analysis between patients with early and late-onset AD, because the severity of iron deposition may differ according to age at onset. Finally, this was a cross-sectional study and longitudinal studies are warranted to further elucidate the pathogenic effects of iron accumulation on AD progression.

Conclusions

In conclusion, we have demonstrated the whole-brain pattern of widespread increases in cortical magnetic susceptibility, which are suggestive of increased iron accumulation, in the cerebral and cerebellum in AD, and their relationship with poor cognitive performance. Increased iron content was found to be associated with cortical atrophy in patients with AD. Our findings show that QSM may be useful for monitoring the disease progression and cognitive severity of AD at the whole-brain level in vivo, and may provide new insights into the application of QSM as a disease biomarker.

Footnote

Reporting Checklist: The authors have completed the STROBE reporting checklist. Available at https://qims.amegroups.com/article/view/10.21037/qims-22-7/rc

Conflicts of Interest: All authors have completed the ICMJE uniform disclosure form (available at https://qims.amegroups.com/article/view/10.21037/qims-22-7/coif). The authors have no conflicts of interest to declare.

Ethical Statement: The authors are accountable for all aspects of the work in ensuring that questions related to the accuracy or integrity of any part of the work are appropriately investigated and resolved. This prospective cross-sectional study was approved by the Ethics Committee of the China–Japan Friendship Hospital. All subjects were informed of this study and provided written informed consent. The study was conducted in accordance with the Declaration of Helsinki (as revised in 2013).

References

1. Alzheimer's Association. 2016 Alzheimer's disease facts and figures. Alzheimers Dement 2016;12:459-509.
2. DeTure MA, Dickson DW. The neuropathological diagnosis of Alzheimer's disease. Mol Neurodegener

4584

Yang et al. Iron deposition related to cognition and brain atrophy in AD

2019;14:32.

3. Telling ND, Everett J, Collingwood JF, Dobson J, van der Laan G, Gallagher JJ, Wang J, Hitchcock AP. Iron Biochemistry is Correlated with Amyloid Plaque Morphology in an Established Mouse Model of Alzheimer's Disease. Cell Chem Biol 2017;24:1205-1215.e3.

4. Yamamoto A, Shin RW, Hasegawa K, Naiki H, Sato H, Yoshimasu F, Kitamoto T. Iron (III) induces aggregation of hyperphosphorylated tau and its reduction to iron (II) reverses the aggregation: implications in the formation of neurofibrillary tangles of Alzheimer's disease. J Neurochem 2002;82:1137-47.

5. Sayre LM, Perry G, Harris PL, Liu Y, Schubert KA, Smith MA. In situ oxidative catalysis by neurofibrillary tangles and senile plaques in Alzheimer's disease: a central role for bound transition metals. J Neurochem 2000;74:270-9.

6. Honda K, Casadesus G, Petersen RB, Perry G, Smith MA. Oxidative stress and redox-active iron in Alzheimer's disease. Ann N Y Acad Sci 2004;1012:179-82.

7. HALLGREN B, SOURANDER P. The effect of age on the non-haemin iron in the human brain. J Neurochem 1958;3:41-51.

8. Aquino D, Bizzi A, Grisoli M, Garavaglia B, Bruzzone MG, Nardocci N, Savoiardo M, Chiapparini L. Age-related iron deposition in the basal ganglia: quantitative analysis in healthy subjects. Radiology 2009;252:165-72.

9. Zecca L, Youdim MB, Riederer P, Connor JR, Crichton RR. Iron, brain ageing and neurodegenerative disorders. Nat Rev Neurosci 2004;5:863-73.

10. Ward RJ, Zucca FA, Duyn JH, Crichton RR, Zecca L. The role of iron in brain ageing and neurodegenerative disorders. Lancet Neurol 2014;13:1045-60.

11. de Rochefort L, Liu T, Kressler B, Liu J, Spincemaille P, Lebon V, Wu J, Wang Y. Quantitative susceptibility map reconstruction from MR phase data using bayesian regularization: validation and application to brain imaging. Magn Reson Med 2010;63:194-206.

12. Schweser F, Deistung A, Lehr BW, Reichenbach JR. Quantitative imaging of intrinsic magnetic tissue properties using MRI signal phase: an approach to in vivo brain iron metabolism? Neuroimage 2011;54:2789-807.

13. Langkammer C, Schweser F, Krebs N, Deistung A, Goessler W, Scheurer E, Sommer K, Reishofer G, Yen K, Fazekas F, Ropele S, Reichenbach JR. Quantitative susceptibility mapping (QSM) as a means to measure brain iron? A post mortem validation study. Neuroimage 2012;62:1593-9.

14. Du L, Zhao Z, Cui A, Zhu Y, Zhang L, Liu J, Shi S, Fu C,

Han X, Gao W, Song T, Xie L, Wang L, Sun S, Guo R, Ma G. Increased Iron Deposition on Brain Quantitative Susceptibility Mapping Correlates with Decreased Cognitive Function in Alzheimer's Disease. ACS Chem Neurosci 2018;9:1849-57.

15. Kim HG, Park S, Rhee HY, Lee KM, Ryu CW, Rhee SJ, Lee SY, Wang Y, Jahng GH. Quantitative susceptibility mapping to evaluate the early stage of Alzheimer's disease. Neuroimage Clin 2017;16:429-38.

16. Cogswell PM, Wiste HJ, Senjem ML, Gunter JL, Weigand SD, Schwarz CG, Arani A, Therneau TM, Lowe VJ, Knopman DS, Botha H, Graff-Radford J, Jones DT, Kantarci K, Vemuri P, Boeve BF, Mielke MM, Petersen RC, Jack CR Jr. Associations of quantitative susceptibility mapping with Alzheimer's disease clinical and imaging markers. Neuroimage 2021;224:117433.

17. Dickerson BC, Bakkour A, Salat DH, Feczko E, Pacheco J, Greve DN, Grodstein F, Wright CI, Blacker D, Rosas HD, Sperling RA, Atri A, Growdon JH, Hyman BT, Morris JC, Fischl B, Buckner RL. The cortical signature of Alzheimer's disease: regionally specific cortical thinning relates to symptom severity in very mild to mild AD dementia and is detectable in asymptomatic amyloid-positive individuals. Cereb Cortex 2009;19:497-510.

18. Kälin AM, Park MT, Chakravarty MM, Lerch JP, Michels L, Schroeder C, Broicher SD, Kollias S, Nitsch RM, Gietl AF, Unschuld PG, Hock C, Leh SE. Subcortical Shape Changes, Hippocampal Atrophy and Cortical Thinning in Future Alzheimer's Disease Patients. Front Aging Neurosci 2017;9:38.

19. Acosta-Cabronero J, Cardenas-Blanco A, Betts MJ, Butryn M, Valdes-Herrera JP, Galazky I, Nestor PJ. The whole-brain pattern of magnetic susceptibility perturbations in Parkinson's disease. Brain 2017;140:118-31.

20. Thomas GEC, Leyland LA, Schrag AE, Lees AJ, Acosta-Cabronero J, Weil RS. Brain iron deposition is linked with cognitive severity in Parkinson's disease. J Neurol Neurosurg Psychiatry 2020;91:418-25.

21. McKhann G, Drachman D, Folstein M, Katzman R, Price D, Stadlan EM. Clinical diagnosis of Alzheimer's disease: report of the NINCDS-ADRDA Work Group under the auspices of Department of Health and Human Services Task Force on Alzheimer's Disease. Neurology 1984;34:939-44.

22. Folstein MF, Folstein SE, McHugh PR. "Mini-mental state". A practical method for grading the cognitive state of patients for the clinician. J Psychiatr Res 1975;12:189-98.

23. Nasreddine ZS, Phillips NA, Bédirian V, Charbonneau S,

Whitehead V, Collin I, Cummings JL, Chertkow H. The Montreal Cognitive Assessment, MoCA: a brief screening tool for mild cognitive impairment. J Am Geriatr Soc 2005;53:695-9.

24. Li W, Wu B, Liu C. Quantitative susceptibility mapping of human brain reflects spatial variation in tissue composition. Neuroimage 2011;55:1645-56.

25. Wu B, Li W, Guidon A, Liu C. Whole brain susceptibility mapping using compressed sensing. Magn Reson Med 2012;67:137-47.

26. Wei H, Dibb R, Zhou Y, Sun Y, Xu J, Wang N, Liu C. Streaking artifact reduction for quantitative susceptibility mapping of sources with large dynamic range. NMR Biomed 2015;28:1294-303.

27. Acosta-Cabronero J, Betts MJ, Cardenas-Blanco A, Yang S, Nestor PJ. In Vivo MRI Mapping of Brain Iron Deposition across the Adult Lifespan. J Neurosci 2016;36:364-74.

28. Fischl B, Dale AM. Measuring the thickness of the human cerebral cortex from magnetic resonance images. Proc Natl Acad Sci U S A 2000;97:11050-5.

29. Fischl B, Sereno MI, Dale AM. Cortical surface-based analysis. II: Inflation, flattening, and a surface-based coordinate system. Neuroimage 1999;9:195-207.

30. Betts MJ, Acosta-Cabronero J, Cardenas-Blanco A, Nestor PJ, Düzel E. High-resolution characterisation of the aging brain using simultaneous quantitative susceptibility mapping (QSM) and R2* measurements at 7T. Neuroimage 2016;138:43-63.

31. Burgetova R, Dusek P, Burgetova A, Pudlac A, Vaneckova M, Horakova D, Krasensky J, Varga Z, Lambert L. Age-related magnetic susceptibility changes in deep grey matter and cerebral cortex of normal young and middle-aged adults depicted by whole brain analysis. Quant Imaging Med Surg 2021;11:3906-19.

32. Rogers JT, Randall JD, Cahill CM, Eder PS, Huang X, Gunshin H, Leiter L, McPhee J, Sarang SS, Utsuki T, Greig NH, Lahiri DK, Tanzi RE, Bush AI, Giordano T, Gullans SR. An iron-responsive element type II in the 5'-untranslated region of the Alzheimer's amyloid precursor protein transcript. J Biol Chem 2002;277:45518-28.

33. Hui Y, Wang D, Li W, Zhang L, Jin J, Ma N, Zhou L, Nakajima O, Zhao W, Gao X. Long-term overexpression of heme oxygenase 1 promotes tau aggregation in mouse brain by inducing tau phosphorylation. J Alzheimers Dis 2011;26:299-313.

34. Jagust W. Imaging the evolution and pathophysiology of Alzheimer disease. Nat Rev Neurosci 2018;19:687-700.

35. Bulk M, Kenkhuis B, van der Graaf LM, Goeman JJ, Natté R, van der Weerd L. Postmortem T2*- Weighted MRI Imaging of Cortical Iron Reflects Severity of Alzheimer's Disease. J Alzheimers Dis 2018;65:1125-37.

36. van Bergen JM, Li X, Hua J, Schreiner SJ, Steininger SC, Quevenco FC, Wyss M, Gietl AF, Treyer V, Leh SE, Buck F, Nitsch RM, Pruessmann KP, van Zijl PC, Hock C, Unschuld PG. Colocalization of cerebral iron with Amyloid beta in Mild Cognitive Impairment. Sci Rep 2016;6:35514.

37. Tiepolt S, Schäfer A, Rullmann M, Roggenhofer E; Gertz HJ, Schroeter ML, Patt M, Bazin PL, Jochimsen TH, Turner R, Sabri O, Barthel H. Quantitative Susceptibility Mapping of Amyloid-β Aggregates in Alzheimer's Disease with 7T MR. J Alzheimers Dis 2018;64:393-404.

38. van Bergen JMG, Li X, Quevenco FC, Gietl AF, Treyer V, Meyer R, Buck A, Kaufmann PA, Nitsch RM, van Zijl PCM, Hock C, Unschuld PG. Simultaneous quantitative susceptibility mapping and Flutemetamol-PET suggests local correlation of iron and β-amyloid as an indicator of cognitive performance at high age. Neuroimage 2018;174:308-16.

39. Farrall AJ, Wardlaw JM. Blood-brain barrier: ageing and microvascular disease--systematic review and meta-analysis. Neurobiol Aging 2009;30:337-52.

40. Klohs J, Deistung A, Schweser F, Grandjean J, Dominietto M, Waschkies C, Nitsch RM, Knuesel I, Reichenbach JR, Rudin M. Detection of cerebral microbleeds with quantitative susceptibility mapping in the ArcAbeta mouse model of cerebral amyloidosis. J Cereb Blood Flow Metab 2011;31:2282-92.

41. Viswanathan A, Greenberg SM. Cerebral amyloid angiopathy in the elderly. Ann Neurol 2011;70:871-80.

42. Damulina A, Pirpamer L, Soellradl M, Sackl M, Tinauer C, Hofer E, Enzinger C, Gesierich B, Duering M, Ropele S, Schmidt R, Langkammer C. Cross-sectional and Longitudinal Assessment of Brain Iron Level in Alzheimer Disease Using 3-T MRI. Radiology 2020;296:619-26.

43. Hametner S, Endmayr V, Deistung A, Palmrich P, Prihoda M, Haimburger E, Menard C, Feng X, Haider T, Leisser M, Köck U, Kaider A, Höftberger R, Robinson S, Reichenbach JR, Lassmann H, Traxler H, Trattnig S, Grabner G. The influence of brain iron and myelin on magnetic susceptibility and effective transverse relaxation - A biochemical and histological validation study. Neuroimage 2018;179:117-33.

44. Seghier ML. The angular gyrus: multiple functions and multiple subdivisions. Neuroscientist 2013;19:43-61.

45. Deschamps I, Baum SR, Gracco VL. On the role of the supramarginal gyrus in phonological processing and verbal working memory: evidence from rTMS studies. Neuropsychologia 2014;53:39-46.

46. Streit WJ, Miller KR, Lopes KO, Njie E. Microglial degeneration in the aging brain--bad news for neurons? Front Biosci 2008;13:3423-38.

47. Horowitz MP, Greenamyre JT. Mitochondrial iron metabolism and its role in neurodegeneration. J Alzheimers Dis 2010;20 Suppl 2:S551-68.

48. Dixon SJ, Lemberg KM, Lamprecht MR, Skouta R, Zaitsev EM, Gleason CE, Patel DN, Bauer AJ, Cantley AM, Yang WS, Morrison B 3rd, Stockwell BR. Ferroptosis: an iron-dependent form of nonapoptotic cell death. Cell 2012;149:1060-72.

49. Xia C, Makaretz SJ, Caso C, McGinnis S, Gomperts SN, Sepulcre J, Gomez-Isla T, Hyman BT, Schultz A, Vasdev N, Johnson KA, Dickerson BC. Association of In Vivo 18FAV-1451 Tau PET Imaging Results With Cortical Atrophy and Symptoms in Typical and Atypical Alzheimer

50. Disease. JAMA Neurol 2017;74:427-36.

51. Mattsson N, Ossenkoppele R, Smith R, Strandberg O, Ohlsson T, Jögi J, Palmqvist S, Stomrud E, Hansson O. Greater tau load and reduced cortical thickness in APOE ε4-negative Alzheimer's disease: a cohort study. Alzheimers Res Ther 2018;10:77.

51. Ayton S, Wang Y, Diouf I, Schneider JA, Brockman J, Morris MC, Bush AI. Brain iron is associated with accelerated cognitive decline in people with Alzheimer pathology. Mol Psychiatry 2020;25:2932-41.

52. Spotorno N, Acosta-Cabronero J, Stomrud E, Lampinen B, Strandberg OT, van Westen D, Hansson O. Relationship between cortical iron and tau aggregation in Alzheimer's disease. Brain 2020;143:1341-9.

53. Gleason A, Bush AI. Iron and Ferroptosis as Therapeutic Targets in Alzheimer's Disease. Neurotherapeutics 2021;18:252-64.

54. Belaidi AA, Bush AI. Iron neurochemistry in Alzheimer's disease and Parkinson's disease: targets for therapeutics. J Neurochem 2016;139 Suppl 1:179-97.